Microstructure, mechanical behavior and low temperature superplasticity of ECAP processed ZM21 Mg alloy

Ehsan Mostaed [a,*], Alberto Fabrizi [b], David Dellasega [c], Franco Bonollo [b], Maurizio Vedani [a]

[a] Department of Mechanical Engineering, Politecnico di Milano, Milan, Italy
[b] Department of Management and Engineering, Università di Padova, Stradella S. Nicola 3, 36100 Vicenza, Italy
[c] Department of Energy, Politecnico di Milano, Milan, Italy

Received 28 January 2015
Received in revised form 26 February 2015
Accepted 3 March 2015
Available online 10 March 2015

1. Introduction

Being the lightest commercial structural metal, with desirable damping capacity, good castability and recyclability, magnesium has been attracting much attention as a potential metallic material in a wide range of automotive, military, electronics and aerospace applications. However, owing to its hexagonal closed-packed (HCP) crystal structure providing limited number of active slip systems, magnesium exhibits poor formability at room temperature [1–3]. Generally, deformation of Mg at room temperature is mainly governed by basal slip $\{0\,0\,0\,1\}\langle 1\,1\,\bar{2}\,0\rangle$ since critical resolved shear stress (CRSS) for the basal slip at room temperature is much lower than those for non-basal slip systems. Basal planes alone provide only two independent slip systems which are much less than the required five independent slip systems to satisfy the Taylor criterion [4], leading to poor ductility of Mg at room temperature. Previous investigations showed that with increasing of temperature, the CRSS of non-basal slip systems decrease gradually while that of basal slip remains constant. Therefore, improved formability of Mg at elevated temperatures (>180 °C) is associated with the activation of non-basal slip systems [5,6]. Moreover, limited active slip systems in Mg results in the formation of a strong crystallographic texture upon conventional thermo-mechanical processing such as rolling and extrusion. Therefore, mechanical properties of wrought Mg alloys are strongly influenced by texture orientation induced by previous forming processes [7–9].

In addition to dislocation slip, magnesium exhibits a strong tendency for twining, especially for $\{1\,0\,\bar{1}\,2\}\langle 1\,0\,\bar{1}\,1\rangle$ extension twin accommodating extension along the *c*-axis. Accordingly, twinning

* Corresponding author. Tel.: +39 02 2399 8661; fax: +39 02 2399 8644.
E-mail address: ehsan.mostaed@polimi.it (E. Mostaed).

in Mg plays a key role in plastic deformation upon contribution to meet the Taylor criterion. Compared to metals with face-centered and body-centered cubic structures, Mg is a low-symmetry material having axial ratio (c/a) of around 1.633 in its crystal lattice [10,11]. As the axial ratio in Mg is less than $\sqrt{3}$, the activation of extension twin is achieved when tensile and compression stresses are perpendicular and parallel to the basal planes, respectively, producing marked tension–compression yield asymmetry [8,12–14]. Tension–compression yield asymmetry restricts Mg alloys from structural applications in which parts are simul-taneously subjected to tension and compression stresses (e.g. in bending or in axial tension–compression cycles). Previous studies showed that the mechanical asymmetry in Mg alloys could be alleviated by several ways such as texture weakening [15], alloying elements [16], heat treatments [17] and grain refinement [15,18–20]. However, among the aforementioned approaches, tex-ture and grain size give significant contributions to the mechanical asymmetric behavior.

In addition, it has been demonstrated that superplastic forming of Mg alloys plays a crucial role and represents a good opportunity for shaping of these materials into complex geometries and into curved parts, for subsequent use in a wide range of applications [21]. Thus, in order to expand their applicability, considerable effort has been devoted to improve the formability of Mg alloys.

Superplasticity generally occurs at high temperatures (above $\sim 0.5\ T_m$, where T_m is the absolute melting temperature of the material), where the plastic flow mechanism is mainly diffusion-controlled. It is accepted that fine grains with size of less than 10 μm are required to obtain superplasticity since the dominant flow process is grain boundary sliding (GBS) [22,23]. Accordingly, several investigations have been carried out on tailoring the microstructure through various plastic deformation methods aimed at improving the superplastic ductility such as extrusion [24], equal channel angular pressing (ECAP) [25] and differential speed rolling (DSR) [26]. Thermo-mechanical processing techniques such as rolling and extrusion are generally used to achieve small grain sizes. However, these techniques cannot attain a grain size smaller than ~2–3 μm. In addition, the mentioned methods generally cause a strong texture in which the basal planes in most grains are distributed parallel to the rolling or extrusion directions, giving rise to deterioration of ductility.

In the last decades, microstructural refinement induced by severe plastic deformation (SPD) techniques has been attracting great attention owing to the possibility of achieving very high mechanical properties in Mg alloys. As a bulk processing method, ECAP is one of the most efficient SPD techniques being able to produce metallic materials with ultra-fine grained (UFG) structures by introducing massive strain during deformation [19,27–34]. Alloys with UFG structure featuring high-angle and non-equilibrium grain boundaries were found to be capable of GBS and exhibit marked superplasticity properties even at high strain rates [35] and/or at low temperatures [36].

In the present work, the possibility of fine tuning texture and properties in a Mg alloy was investigated in order to extensively improve plasticity. An UFG ZM21 Mg alloy with an equiaxed grain structure and particular basal plane orientation was produced through a multi-stage ECAP method showing very high superplasticity and limited mechanical asymmetry.

2. Experimental procedure

2.1. Materials and method

In the present work, a commercial ZM21 alloy provided by SHL-ALUBIN company (Mg–1.78Zn–0.89Mn, wt.%) in the form of extruded bar was investigated. Cylindrical specimens of 10 mm in diameter with a length of 100 mm were machined from the extruded bars for further processing. ECAP was conducted using a die featuring two cylindrical channels of 10 mm in diameter, intersecting at an angle of 110° and with an outer arc of curvature of 20°. According to the Iwahashi equation [37], this geometry involves an equivalent shear strain of 0.76 per each pass. ECAP processing consisted of two stages, at 200 and 150 °C, where 4 passes were performed. Table 1 summarizes the conditions investigated for the ZM21 alloy at the different ECAP temperatures. All the samples were subjected to repetitive pressings and rotated by 90° in the same direction between each pass according to the procedure designated as route B_C in the literature [38]. Samples were sprayed with MoS_2 lubricant and pressed into the ECAP die at a speed of 30 mm/min.

Table 1
ECAP processing conditions of the investigated samples.

Sample code	Sample condition
A0	As-extruded ZM21 Mg alloy
A4	ECAP treated for 4 passes at 200 °C
B4	A4 + ECAP treated for 4 passes at 150 °C

2.2. Microstructural and texture characterization

Microstructural examination of the all samples was characterized by Electron Backscattered Diffraction (EBSD) technique in a plane perpendicular to the pressing direction. In particular, distribution of grain size, crystallographic texture and grain orientation maps of the ZM21 alloy in the as-received condition and after ECAP process were obtained using EBSD technique interfaced with a Field Emission Gun Scanning Electron Microscope (FEG-SEM). All the data were then processed with TSL OIM™ software. The typical scan area was 30 μm × 30 μm with a 0.2 μm step size for the ECAP-processed specimens, while, in order to achieve good statistical data due to the presence of coarser grains, a larger scan area was selected for as-received alloy samples. Prior to EBSD analysis, all specimens' surfaces were carefully prepared by standard mechanical polishing followed by low-angle ion milling. The fracture surfaces of all samples at different temperatures of tensile tests were also examined using FEG-SEM.

2.3. Mechanical characterization

Mechanical properties were evaluated by tensile and compression tests. Standard deviations were calculated in each case out of a population of three experiments. Following ASTM E8-04 [39] tensile specimens with a gage length of 12 mm and a diameter of 4 mm were machined along the longitudinal direction of the ECAP billets and tested at room temperature (RT) and at 150 ° C. Moreover, characterization of the superplastic behavior was carried out at 200 °C with strain rates ranging from $5.0 \times 10^{-4}\ s^{-1}$ to $1.0 \times 10^{-2}\ s^{-1}$. Compression tests were carried out at room temperature at a strain rate of $1 \times 10^{-3}\ s^{-1}$on cylindrical specimens with diameter of 10 mm and height of 20 mm according to ASTM E9-09 specifications [40], cut along the axial direction of the as-extruded and ECAP processed billets.

3. Results and discussion

3.1. Microstructural characterization

Fig. 1 shows EBSD maps and corresponding grain size distribution of all the investigated samples. The color code of all the figures is given by the reference sector at the bottom left corner of the images. As seen in Fig. 1a and b, the extruded samples (A0) exhibit a heterogeneous microstructure with a bimodal grain size distribution with different coarse-grain sizes (5–60 μm) and contain considerable fraction of grains ranging from 10 to 30 μm. However, after the first stage of ECAP (A4 samples) the initial grain structure was remarkably refined, resulting in a microstructure consisting of fine and equiaxed grains with a size distribution from 0.3 to 3 μm and an average grain size of 0.7 μm (Fig. 1c and d). Thus, it should be noted that ECAP process led to a considerable grain refinement in the alloy through dynamic recrystallization (DRX) mechanism. Interestingly, as depicted in Fig. 1e and f, with an additional 4 ECAP passes at 150 °C (second stage of processing, B4 samples) not only no further grain refinement occurred, but also a slight grain growth was observed, from 0.7 to 0.9 μm. The observed grain coarsening can be attributed to the relatively high interpass time spent at processing temperature and lower propensity to recrystallization given by the small grain size structure. A

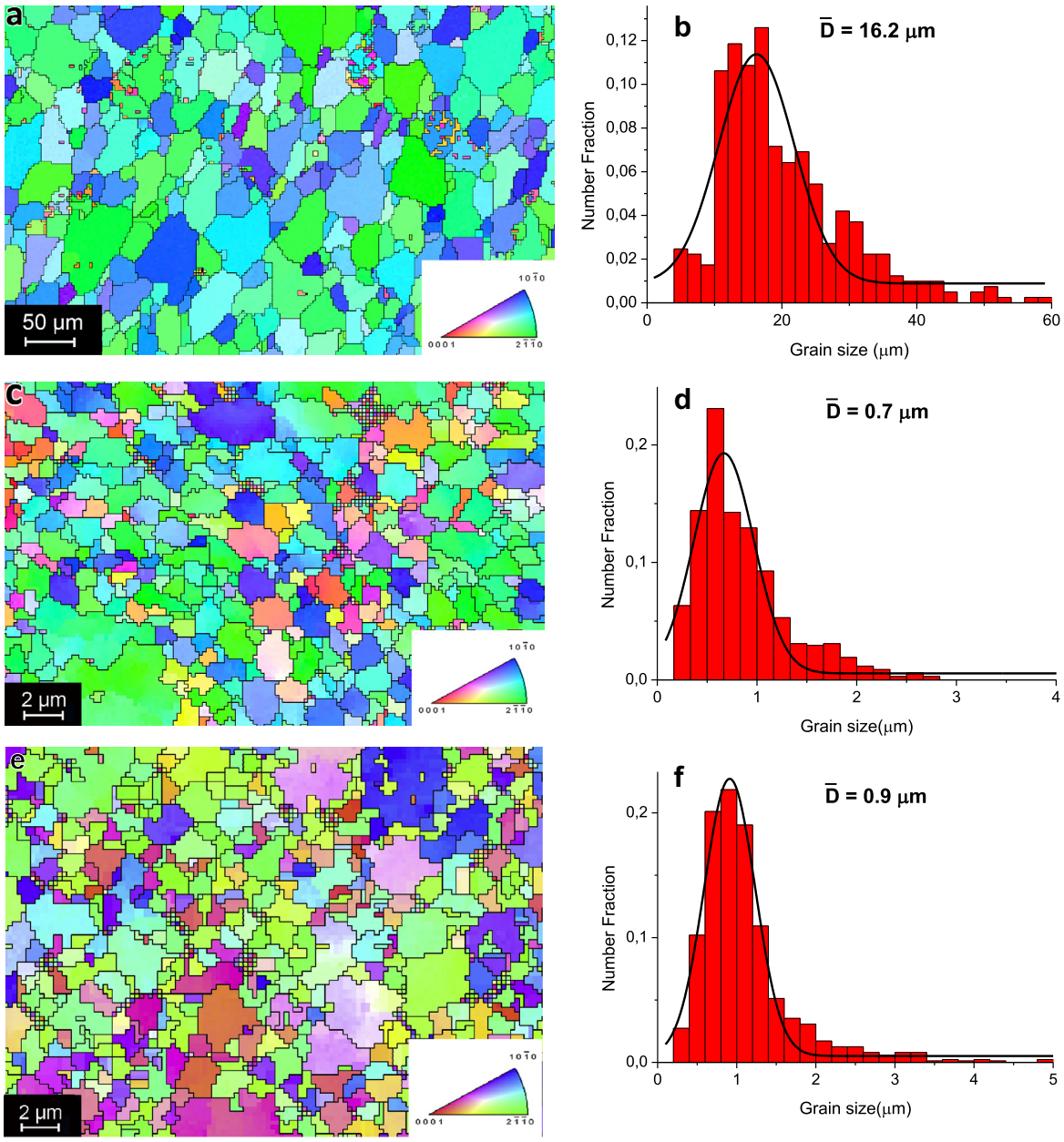

Fig. 1. EBSD image orientation maps and corresponding grain size distribution of (a and b) A0, (c and d) A4 and (e and f) B4 samples.

similar increase in the average grain size was also reported in other research works [19,41]. Moreover, the activation energy for grain growth in fine-grained Mg alloys is markedly lower than that of coarse-grained alloys [42]. The mentioned difference in the activation energy could be even more pronounced in the case of UFG Mg alloys since the grain boundaries of the UFG materials are in a non-equilibrium state and are more likely to change to the equilibrium state, leading to a slight increment of grain size in B4 samples.

Fig. 2 represents the {0 0 0 2} pole figure of the investigated samples. It is apparent from Fig. 2a that the A0 samples exhibit a typical extrusion direction (ED) $\|\langle 10\bar{1}0\rangle$ fiber texture as basal planes in most grains are distributed parallel to the extrusion direction. After 4 passes of ECAP processing (Fig. 2b), the dominant texture with basal planes parallel to ED became weaker, however the strongest component with basal planes parallel to the ED almost remained. As A0 samples underwent the first stage of ECAP, the maximum texture intensity increased from 8 to 14. After 4 more passes at 150 °C (B4 samples), the original fiber texture was almost completely replaced by a new one featuring the alignment of the basal planes along the ECAP shear planes. The basal pole distribution formed a maximum component locating at about 53° from TD (transverse direction) towards ED. However, the maximum texture intensity of {0 0 0 2} pole figure for B4 samples decreased to about 10.

Fig. 3 shows the distribution of Schmid factor for $(0001)\langle 11\bar{2}0\rangle$ basal slip in the as-extruded and ECAP processed samples. As seen, with ECAP advancement the value of Schmid factor invariably increases, leading to a remarkable improvement, from 0.11 (A0) to 0.20 and 0.32 for A4 and B4 samples, respectively.

Since at room and moderately elevated temperatures plastic deformation is mostly governed by the basal slip [43], the Schmid factor value for this slip system is supposed to play a criti-cal role in mechanical behavior of Mg alloys. For B4 samples, the rotation of the basal planes to ED (which is the tensile axis) brought about a significantly higher value of basal slip Schmid fac-tor of 0.32 (Fig. 3c) which is favorable for the operation of basal

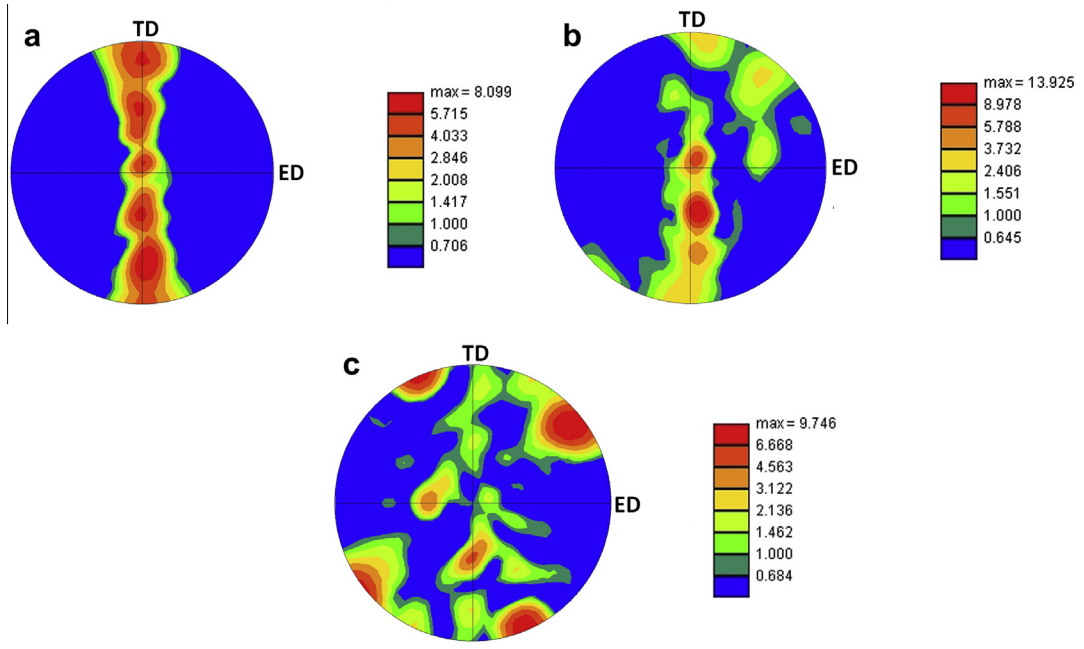

Fig. 2. (0002) Pole figures showing the crystallographic texture of sample (a) A0, (b) A4 and (c) B4.

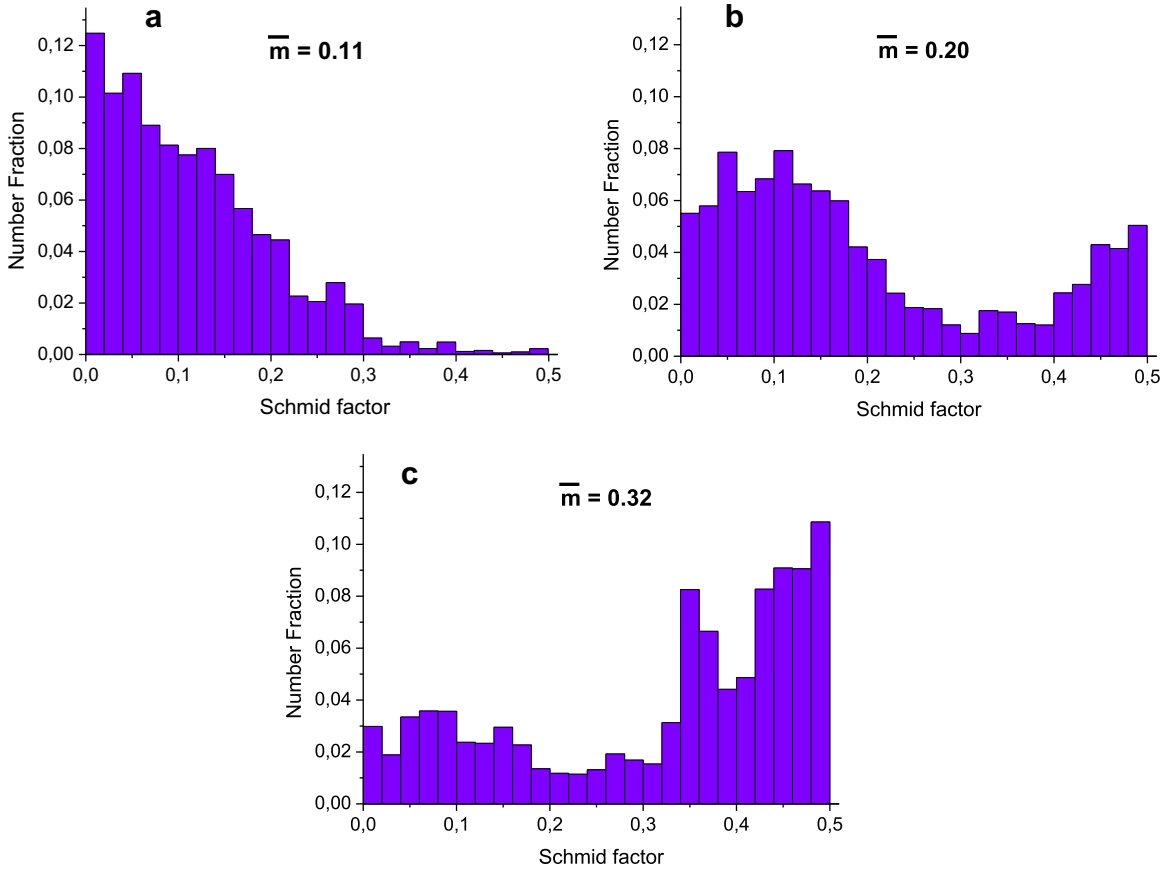

Fig. 3. Distribution of Schmid factors for basal slip in the (a) A0, (b) A4 and (c) B4 samples.

slip, lowering the stress required for yielding. In other words, among all investigated samples, B4 shows much more favorable texture orientation for dislocation glide on the slip plane (0002), thereby setting favorable conditions for improved ductility properties at room temperature.

3.2. Mechanical characterization

3.2.1. Mechanical properties at room temperature

Fig. 4a and b show the tensile and compressive stress–strain curves of the investigated samples. Data for tensile yield stress

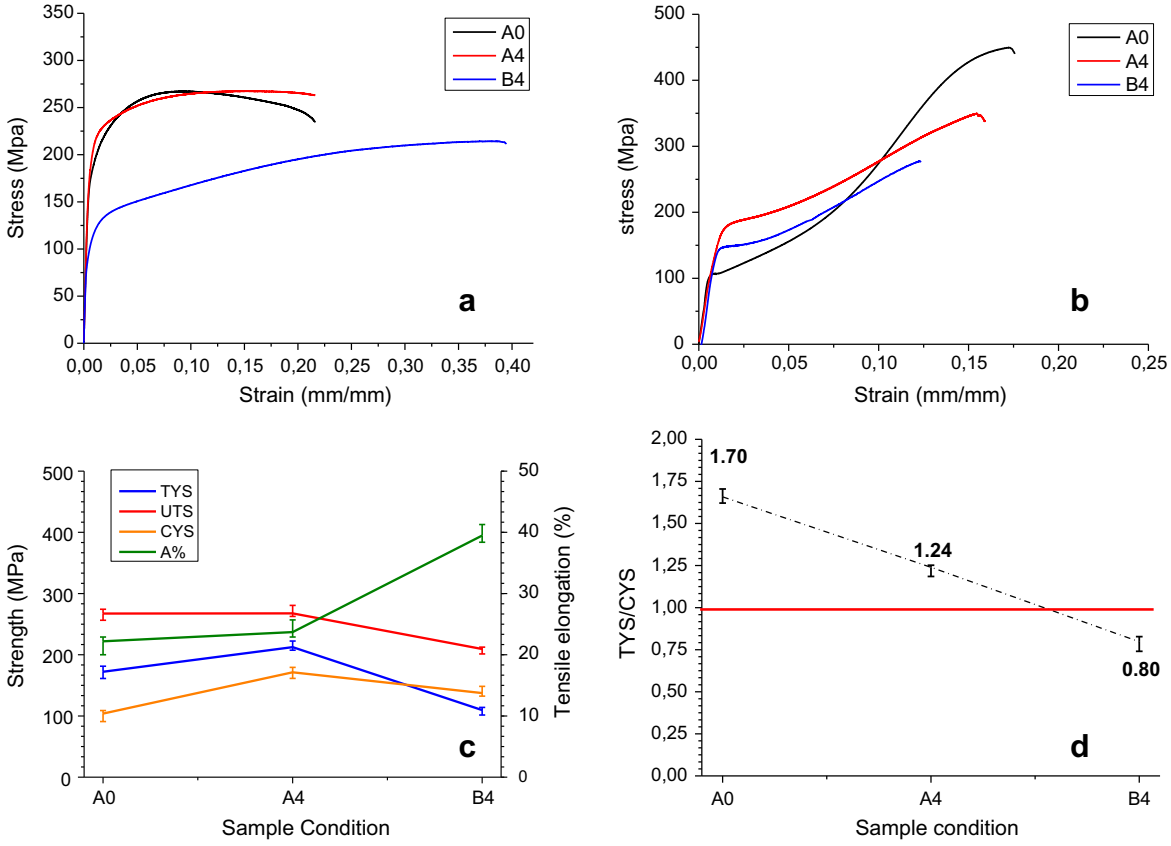

Fig. 4. (a) Tensile, (b) compressive engineering stress–strain curves measured at room temperature, (c) tensile and compression properties and (d) yielding asymmetry of all the investigated samples.

(TYS), ultimate tensile strength (UTS), compressive yield stress (CYS) and tensile fracture elongation (A%) are plotted in Fig. 4c and summarized in Table 2. It can be seen that due to the marked grain refinement from A0 (16 μm) to A4 (0.7 μm) condition, TYS increased from 172 to 212 MPa. However, no obvious change in UTS and fracture elongation was detected. It should be noted that this strengthening effect is measured despite a weaker initial fiber texture as well as higher Schmid factor were found in A4 samples. Therefore, it can be stated that the dominant mechanism for A4 samples was grain refinement strengthening, leading to a net increase in TYS. In case of B4 samples, interestingly, both TYS and UTS remarkably dropped from 212 and 268 MPa down to 110 and 209 MPa, respectively. Nevertheless, elongation to failure considerably increased, from about 24% to 40%. It is suggested that decrease in tensile strength and improvement of uniform elongation are attributed to the formation of the new basal texture, by which basal planes in most grains were tilted towards ED, with notably higher basal slip Schmid factor value, resulting in lower yield stress as well as easier basal slip during the plastic deformation process. In other words, considering A4 and B4 samples with almost similar grain size, the Hall–Petch effect alone is obviously inadequate for explaining the extent of the tensile strength drop. Therefore, it could be concluded that the texture development is the prevailing factor in B4 samples, overwhelming the grain refinement strengthening effect and causing a net decrease in both TYS and UTS and a concurrent substantial improvement of fracture elongation. Furthermore, the remarkable strain hardening exponent value measured in B4 samples (n = 0.27 in contrast to 0.16 and 0.13 for A0 and A4 samples, respectively) strongly supports the hypothesis that other non-basal slip systems were active dur-ing tensile testing.

Table 2
Room temperature mechanical proprieties of the investigated samples.

Sample code	TYS (MPa)	UTS (MPa)	CYS (MPa)	A (%)
A0	172 ± 8	267 ± 8	104 ± 9	22 ± 2
A4	212 ± 7	268 ± 9	171 ± 7	24 ± 1
B4	110 ± 6	209 ± 6	137 ± 8	40 ± 1

Fig. 5 represents SEM fractographs of the investigated tensile samples tested at room temperature. On the fracture surface of A0 samples a large number of cleavage planes and dimples are apparent (Fig. 5a), suggesting a mixed fracture mode of ductile–brittle type. Also for A4 samples, the combination of dimples and cleavage planes is obvious, even though the size of the dimples is much smaller than that found in A0 condition, which is due to the UFG structure (Fig. 5b). In case of B4 samples (see Fig. 5c), a large number of very fine dimples separated by sharp ridges becomes obvious, confirming a remarkable ductile fracture behavior.

Fig. 4b depicts the compressive stress–strain curves of all the samples. Due to the initial fiber texture with the majority of the basal planes lying parallel to the compression axis, resulting in generation of $\{1\,0\,\bar{1}\,2\}\langle 1\,0\,\bar{1}\,1\rangle$ twins [8], samples A0 show a very low CYS of about 104 MPa. As shown in Fig. 4d, this low value of CYS led to a considerably high yielding asymmetry ratio (AR), which is the ratio of the tensile to compression yield stress, of about 1.70. The aforementioned ratio significantly decreased to 1.24 and to 0.80 for A4 and B4 samples, respectively. Indeed, the more symmetric behavior of A4 samples is due to the higher increasing rate of twinning stress than that of slip achieved with the decrease of grain size thus, making twinning less favorable

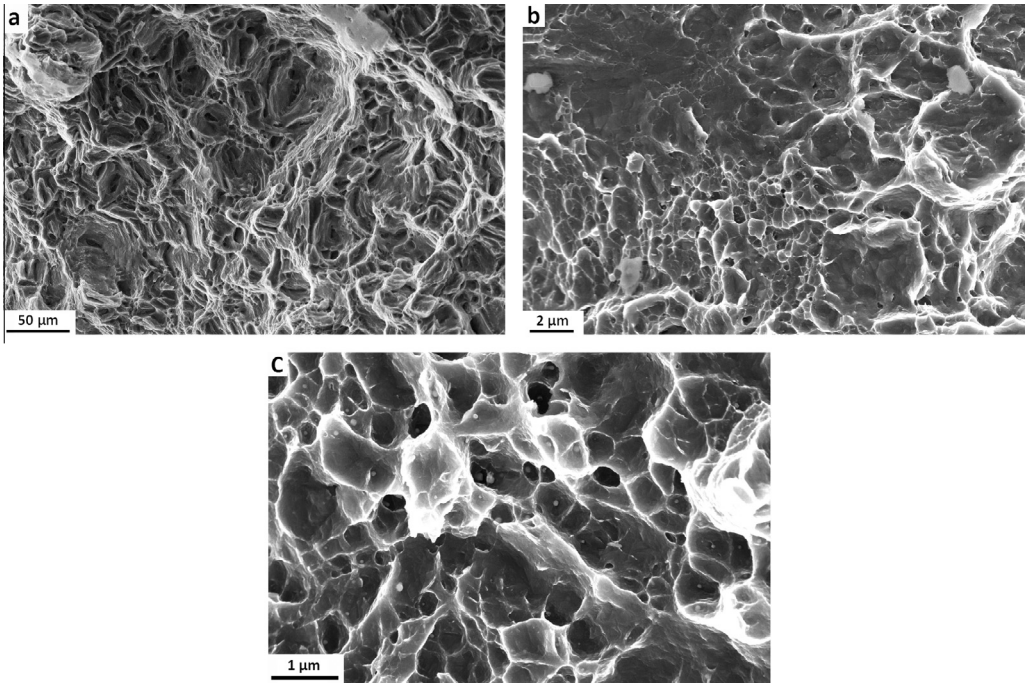

Fig. 5. SEM views of the fracture surfaces of tensile broken samples: (a) A0, (b) A4 and (c) B4.

[44]. This behavior eventually leads to similar tensile and compression yield strength performance (increment of CYS). However, for B4 samples another effective contributor, which is related to the particular basal plane orientation was also included, leading to significant reduction of both TYS and CYS [15].

3.2.2. Mechanical properties at elevated temperatures

Fig. 6 shows the tensile true stress versus true strain curves of all the samples at a strain rate of $1.0 \times 10^{-3}\ s^{-1}$, at 150 and 200 °C. At 150 °C (Fig. 6a), A0 sample shows an extensive strain hardening and sharp drop of flow stress after reaching the peak stress. In case of A4, since at elevated temperatures the tensile behavior becomes more diffusion-controlled, especially in the regime of plastic flow, the flow stress decreases form 180 (for A0) to 148 MPa. As seen, although grain refinement led to con-siderable reduction of the strain hardening, the flow stress drop is still sharp. Moreover, the elongation to failure increased from 80% to 95% for A0 and A4 samples, respectively. For the B4, the flow stress drops significantly while the plastic flow region expands over higher strain ranges, leading to a peak stress and elongation of 88 MPa and 148%, respectively. As discussed in the previous sections, both A4 and B4 samples exhibited almost equal grain size (0.7 μm versus 0.9 μm) but different basal texture orientation. Therefore, texture is considered to be the only responsible for the observed lower flow stress and higher elongation in B4. Indeed, it could be concluded that GBS was not actively operated during the tensile deformation at 150 °C and the dominant mechanism was dislocation slip. Therefore, at this temperature, texture plays a dominant role on the mechanical properties of ZM21 Mg alloy.

Fig. 7 shows the failure surface morphology of the samples tested at 150 ° C at a strain rate of $1.0 \times 10^{-3}\ s^{-1}$. As seen in Fig. 7a, compared to its fracture surface after failure at room tem-perature (see Fig. 5a), the number of observed dimples on the frac-ture surface of A0 increased with the improved ductile behavior. For A4, the average size of dimples decreased while their depth increased, indicating an enhancement of plasticity after ECAP at this temperature (Fig. 7b). In contrast, in B4, a macroscopic shear fracture at about 45° to the tensile axis was found. Fig. 7c clearly

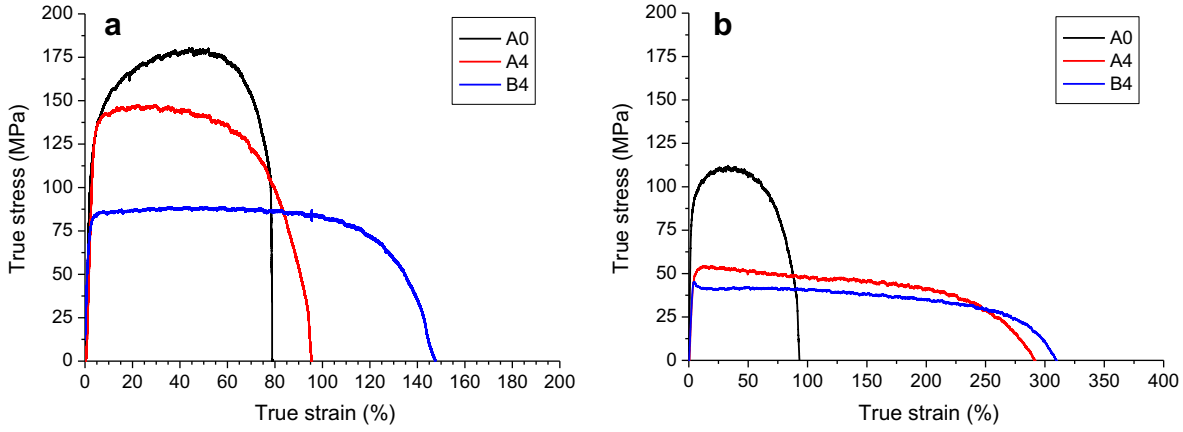

Fig. 6. The true stress versus true strain curves of the samples tested at strain rate of $1.0 \times 10^{-3}\ s^{-1}$ and different temperatures: (a) 150 °C and (b) 200 °C.

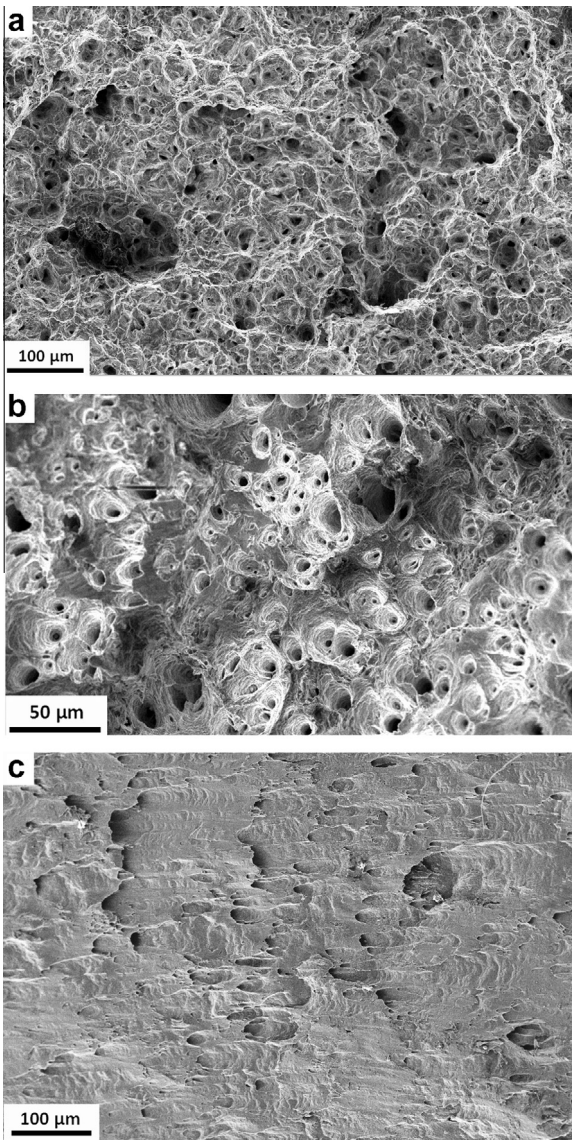

Fig. 7. SEM fractographs of tensile samples broken at 150 °C and at strain rate of $1.0 \times 10^{-3}\ s^{-1}$: samples (a) A0, (b) A4 and (c) B4.

shows the appearance of shear planes on the fracture surface, suggesting that the dominant deformation mechanism for this sample was slipping due to the favorable basal plane orientation for dislocation slip.

Fig. 6b shows the true stress versus true strain curves for all the investigated samples tested at 200 °C and at a strain rate of $1.0 \times 10^{-3}\ s^{-1}$. As seen, for the UFG samples the flow stress fea-tures a clear plateau after yielding, extending over very high strain values. In other words, with a decrease in grain size, both the strain hardening rate and the level of the flow stress considerably decreased, while the elongation significantly increased from 93%to 290% and 310% for A0, A4 and B4 samples, respectively.

It is observed from Fig. 6b that B4 has a lower flow stress than A4 (45 MPa versus 54 MPa), suggesting that the peak flow stress is still mainly texture dependent. It should be noted that compared to the tensile results at 150 °C, the difference in elongation between A4 and B4 is less considerable, confirming that at 200 °C texture has a subtle contribution on the fracture elongation of UFG Mg alloys. That is, the elongation has noticeable grain size dependence since the UFG structure of samples A4 and B4 provides extensive amount of grain boundaries to take part in GBS, which is the dominant mechanism at this temperature and superplastic flow. Hence, GBS was responsible for the notable improvement of elongation in ECAP processed samples at 200 °C and a strain rate of $1.0 \times 10^{-3}\ s^{-1}$.

The fracture surface morphology of all the samples tested at 200 °C and at initial strain rate of $1.0 \times 10^{-3}\ s^{-1}$ is depicted in Fig. 8. As shown in Fig. 8a, even in A0, a large number of deep dim-ples are evident with heterogeneous size distribution, arising from the initial bimodal grain structure (as seen in Fig. 1a). In case of A4 (Fig. 8b), the fracture surface is almost completely covered by a number of dense and deep dimples with tearing ridges. These fea-tures are believed to be a clear indication for an enhancement of plasticity after ECAP at this temperature. Fig. 8c shows that for B4 samples, even at this temperature, a large number of shearing planes on the fracture surface is still visible, indicating a significant contribution of dislocation slip in deformation even at 200 °C. SEM

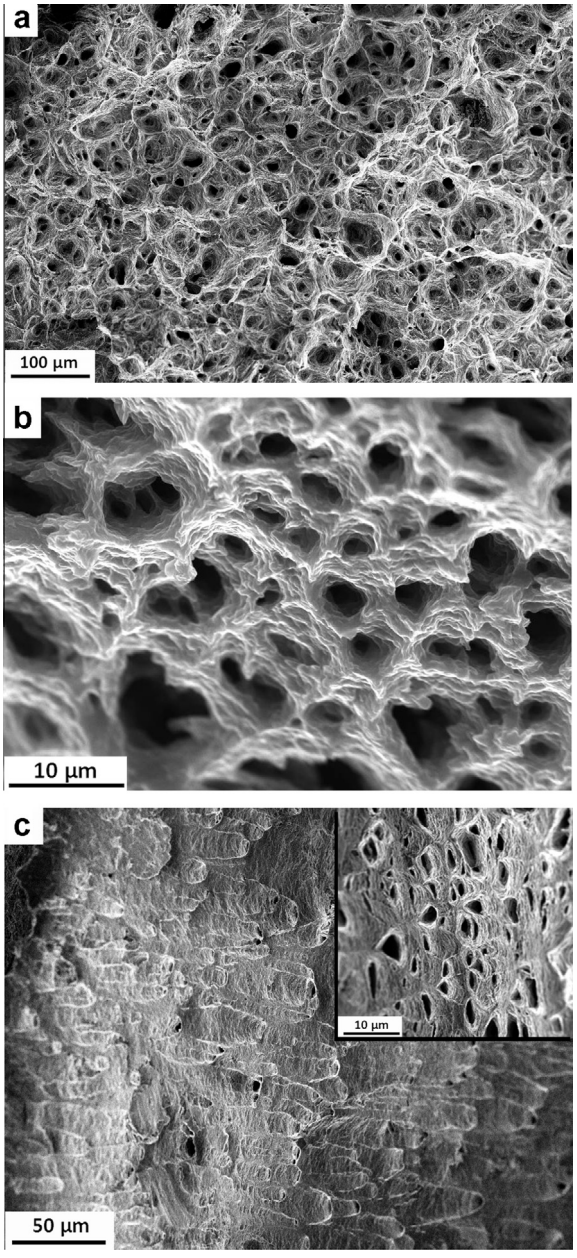

Fig. 8. SEM fractograph of tensile samples broken at 200 °C and at strain rate of $1.0 \times 10^{-3}\ s^{-1}$: samples (a) A0, (b) A4 and (c) B4.

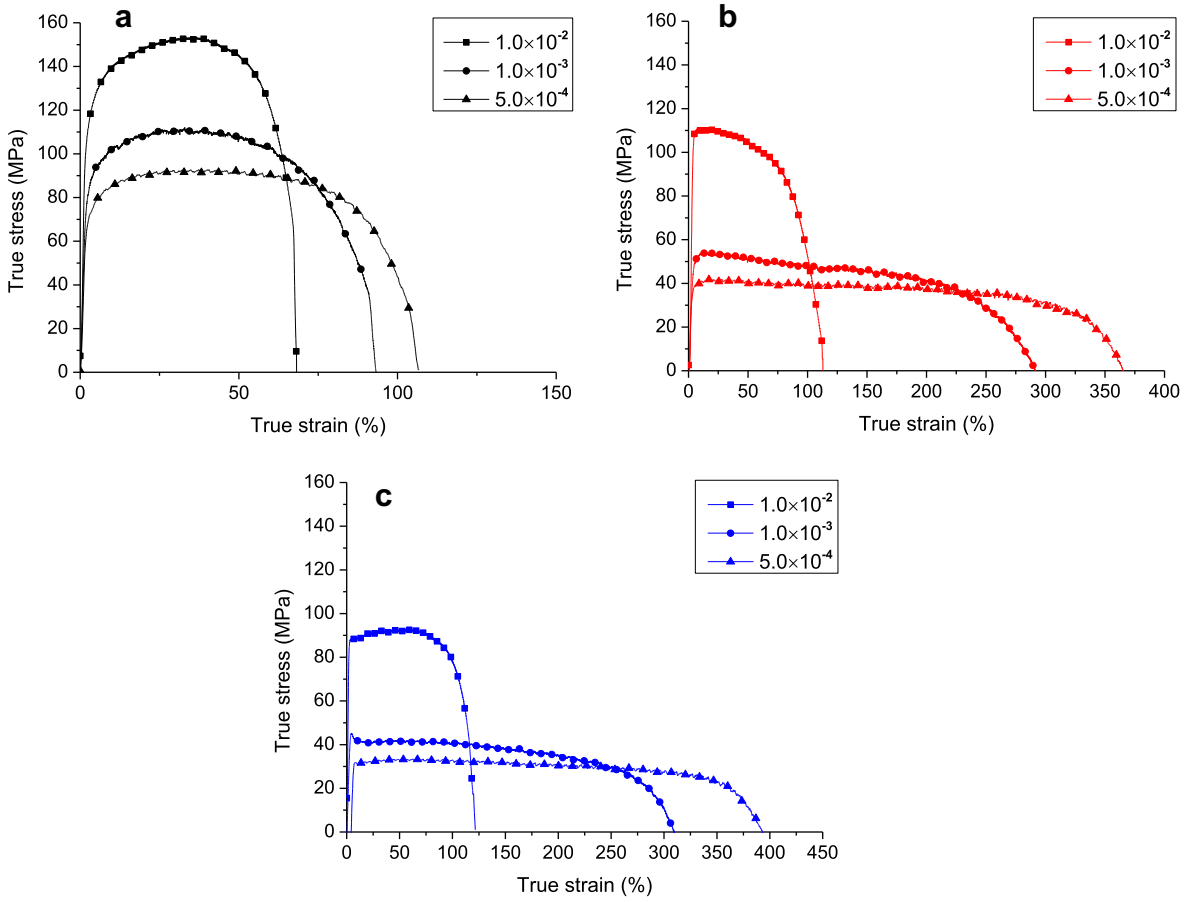

Fig. 9. Effect of strain rate on the true stress versus true strain curves for (a) A0, (b) A4 and (c) B4 samples.

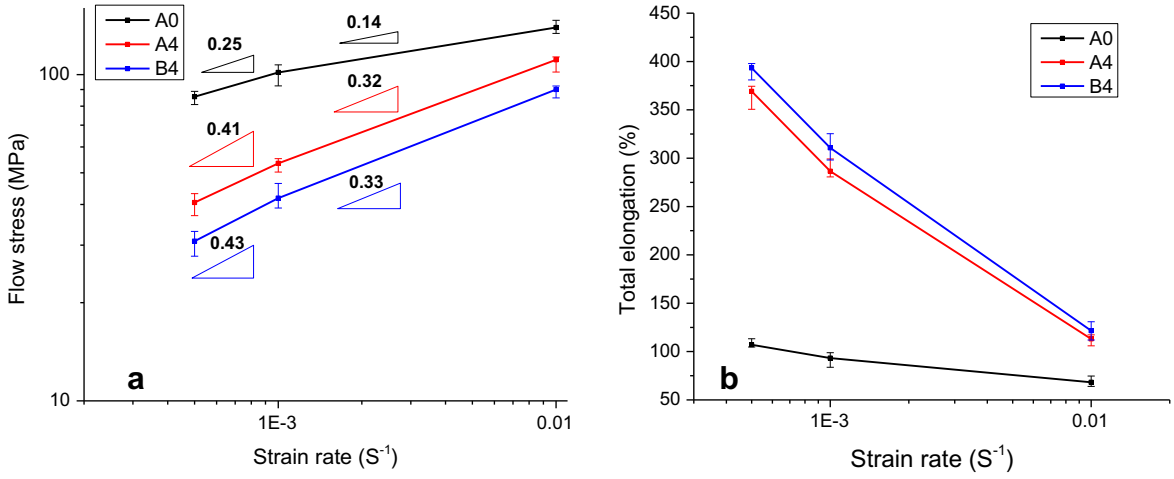

Fig. 10. Variation of (a) flow stress and (b) elongation-to-failure versus strain rate for A0, A4 and B4 samples.

image of a surface perpendicular to the shearing planes is shown in the inset on the top corner of Fig. 8c. As seen, this surface is nearly full of small size plastic dimples, implying remarkable ductility, which corresponds to a measured tensile elongation of about 310%. Accordingly, it could be concluded that at 200 °C flow stress was notably texture dependent, while ductility was strongly influenced by grain size, appearing only in UFG samples.

Fig. 9 shows the typical true stress versus true strain curves at 200 ° C and strain rates ranging from 5.0×10^{-4} s^{-1} to 1.0×10^{-2} s^{-1} for the as-extruded and the ECAP processed alloys.

As expected, for all specimens, the flow stress is dependent on the strain rate. Typically, in all cases, the strain hardening rate and the flow stress decrease with decreasing strain rate and remarkably high ductility was recorded at the lowest strain rates investigated with a nearly constant flow stress. To discuss the results from these curves in perspective, a full summary of all of the tensile properties are given in Fig. 10 where the results of all the samples are plotted against the strain rate.

Fig. 10a shows the variation of flow stress versus the initial strain rate, where the flow stress for each strain rate is determined

at a strain of ε = 0.1. As seen, the flow stress constantly increases with increasing the strain rate. It is well known that for the superplastic alloys the strain rate sensitivity exponent (m), defined as the slope in a double logarithmic plot of flow stress versus strain rate, should be above 0.4 [45]. It can be clearly seen that with decreasing the strain rate the m value increases. For A4 and B4 maximum m values of 0.41 and 0.43 at strain rate of $5.0 \times 10^{-4}\,s^{-1}$ were achieved, respectively. Thus, such a high value of m for UFG samples supports the hypothesis that slip-ac-commodated GBS dominates the deformation. The same increasing trend of m with strain rate was also observed for A0 samples, reaching a value of 0.25 at the strain rate of $5.0 \times 10^{-4}\ s^{-1}$. At higher strain rate the m value was reduced to 0.14, 0.32 and 0.33 for A0, A4 and B4, respectively, suggesting that the rate controlling deformation process at higher strain rates was dislocation slip. Lower placement of B4 plot compared to A4 at all strain rates in Fig. 10a emphasizes the favorable texture orientation for basal slip, requiring a lower stress for plastic flow.

Fig. 10b depicts the elongation to failure of the tested samples at 200 °C, plotted as a function of strain rate. The elongations of all the samples tend to increase with decreasing strain rate. However, compared to A0, this trend is more pronounced for A4 and B4 samples. It is worth mentioning that due to absence of GBS and preferential basal texture orientation during the deformation of A0, its failure elongation lies always remarkably below those of A4 and B4. Maximum elongation values of nearly 370 and 393% were achieved at strain rate of $5.0 \times 10^{-4}\ s^{-1}$ for A4 and B4 samples, respectively, indicating that the UFG alloys exhibit notable superplastic behavior induced by effective contribution of GBS.

It is also apprehensible that even though at room temperature and 150 °C texture dependence on elongation was completely apparent, at 200 °C this dependency was to a large extent undermined by grain size effect, leading to superplastic ductility in UFG samples.

4. Conclusion

In this study, ECAP processing was carried out on ZM21 Mg alloy aimed at achieving ultra-fine grain structure according to a two-stage strategy carried out at decreasing pressing temperature levels, of 200 and 150 °C. Plastic behavior, mechanical asymmetry and low temperature superplasticity of UFG alloy were investigated with the main focus on microstructural and texture evolution. The findings can be summarized as follows:

1. After 4 ECAP passes at 200 °C, remarkable grain refinement was obtained, leading to a homogenous ultrafine grain structure with average size of 700 nm. Although, additional 4 passes at 150 °C could not further refine the microstructure, the initial fiber texture gradually evolved into a new one featuring the preferential alignment of the basal planes along the ECAP shear planes with a higher Schmid factor value.
2. Microstructural and texture characterizations revealed that after the first ECAP stage a clear grain refinement and fiber texture weakening occurred, leading to a net increase in tensile strength. However, after the second stage, due to the formation of the new basal texture tilted towards ECAP direction with notably higher basal slip Schmid factor of 0.32, considerable reduction of yield stress from 212 to 110 MPa and improvement of the fracture elongation from 20% to 40% were achieved.
3. Tensile and compression tests at room temperature revealed that yielding asymmetry can be alleviated by either weakening of basal plane fiber texture or by grain refinement.
4. The stress–strain curves at 150 °C showed that texture is a crucial factor affecting plastic flow and elongation. Accordingly, grain boundary sliding (GBS) was not actively operated during the tensile deformation and the dominant mechanism was dislocation slip.
5. The stress–strain curves at 200 °C showed that the effect of texture on fracture elongation of UFG alloys became minor. In contrast, the impact of grain size became more important, so that UFG samples exhibited maximum elongation above 370% at a strain rate of $5.0 \times 10^{-4}\ s^{-1}$. Therefore, it was suggested that flow stress had noticeable dependence on the texture, while superplastic ductility was strongly dictated by grain size, appearing only in UFG samples.

References

[1] B.L. Mordike, T. Ebert, Magnesium: properties—applications—potential, Mater. Sci. Eng. A 302 (2001) 37–45, http://dx.doi.org/10.1016/S0921-5093(00)01351-4.

[2] Y. Chino, K. Kimura, M. Mabuchi, Twinning behavior and deformation mechanisms of extruded AZ31 Mg alloy, Mater. Sci. Eng. A 486 (2008) 481–488, http://dx.doi.org/10.1016/j.msea.2007.09.058.

[3] S.E. Ion, F.J. Humphreys, S.H. White, Dynamic recrystallisation and the development of microstructure during the high temperature deformation of magnesium, Acta Metall. 30 (1982) 1909–1919, http://dx.doi.org/10.1016/0001-6160(82)90031-1.

[4] M.H. Yoo, Slip, twinning, and fracture in hexagonal close-packed metals, Metall. Trans. A 12 (1981) 409–418, http://dx.doi.org/10.1007/BF02648537.

[5] B. Srinivasarao, N.V. Dudamell, M.T. Pérez-Prado, Texture analysis of the effect of non-basal slip systems on the dynamic recrystallization of the Mg alloy AZ31, Mater. Charact. 75 (2013) 101–107, http://dx.doi.org/10.1016/j.matchar.2012.10.002.

[6] B.C. Wonsiewicz, Plasticity of Magnesium Crystals, Ph.D. Thesis, Massachusetts Institute of Technology, 1966 <http://dspace.mit.edu/handle/1721.1/27989> (accessed 21.02.15).

[7] G. Garcés, P. Pérez, P. Adeva, Effect of the extrusion texture on the mechanical behaviour of Mg–SiCp composites, Scr. Mater. 52 (2005) 615–619, http://dx.doi.org/10.1016/j.scriptamat.2004.11.024.

[8] S. Kleiner, P.J. Uggowitzer, Mechanical anisotropy of extruded Mg–6% Al–1% Zn alloy, Mater. Sci. Eng. A 379 (2004) 258–263, http://dx.doi.org/10.1016/j.msea.2004.02.020.

[9] A. Prakash, S.M. Weygand, H. Riedel, Modeling the evolution of texture and grain shape in Mg alloy AZ31 using the crystal plasticity finite element method, Comput. Mater. Sci. 45 (2009) 744–750, http://dx.doi.org/10.1016/j.commatsci.2008.06.015.

[10] M.M. Avedesian, H. Baker, ASM Specialty Handbook: Magnesium and Magnesium Alloys, ASM International, 1999.

[11] S.X. Song, J.A. Horton, N.J. Kim, T.G. Nieh, Deformation behavior of a twin-roll-cast Mg–6Zn–0.5Mn–0.3Cu–0.02Zr alloy at intermediate temperatures, Scr. Mater. 56 (2007) 393–395, http://dx.doi.org/10.1016/j.scriptamat.2006.10.040.

[12] S.R. Agnew, M.H. Yoo, C.N. Tomé, Application of texture simulation to understanding mechanical behavior of Mg and solid solution alloys containing Li or Y, Acta Mater. 49 (2001) 4277–4289, http://dx.doi.org/10.1016/S1359-6454(01)00297-X.

[13] E.A. Ball, P.B. Prangnell, Tensile-compressive yield asymmetries in high strength wrought magnesium alloys, Scr. Metall. Mater. 31 (1994) 111–116, http://dx.doi.org/10.1016/0956-716X(94)90159-7.

[14] Y.N. Wang, J.C. Huang, The role of twinning and untwinning in yielding behavior in hot-extruded Mg–Al–Zn alloy, Acta Mater. 55 (2007) 897–905, http://dx.doi.org/10.1016/j.actamat.2006.09.010.

[15] S.M. Yin, C.H. Wang, Y.D. Diao, S.D. Wu, S.X. Li, Influence of grain size and texture on the yield asymmetry of Mg–3Al–1Zn alloy, J. Mater. Sci. Technol. 27 (2011) 29–34, http://dx.doi.org/10.1016/S1005-0302(11)60021-2.

[16] J. Bohlen, P. Dobroň, J. Swiostek, D. Letzig, F. Chmelík, P. Lukáč, et al., On the influence of the grain size and solute content on the AE response of magnesium alloys tested in tension and compression, Mater. Sci. Eng. A 462 (2007) 302–306, http://dx.doi.org/10.1016/j.msea.2006.02.470.

[17] J. Jain, W.J. Poole, C.W. Sinclair, M.A. Gharghouri, Reducing the tension–compression yield asymmetry in a Mg–8Al–0.5Zn alloy via precipitation, Scr. Mater. 62 (2010) 301–304, http://dx.doi.org/10.1016/j.scriptamat.2009.11.024.

[18] L.L. Chang, Y.N. Wang, X. Zhao, M. Qi, Grain size and texture effect on compression behavior of hot-extruded Mg–3Al–1Zn alloys at room temperature, Mater. Charact. 60 (2009) 991–994, http://dx.doi.org/10.1016/j.matchar.2009.04.001.

[19] E. Mostaed, M. Hashempour, A. Fabrizi, D. Dellasega, M. Bestetti, F. Bonollo, et al., Microstructure, texture evolution, mechanical properties and corrosion behavior of ECAP processed ZK60 magnesium alloy for biodegradable

applications, J. Mech. Behav. Biomed. Mater. 37 (2014) 307–322, http://dx.doi.org/10.1016/j.jmbbm.2014.05.024.
[20] D.L. Yin, J.T. Wang, J.Q. Liu, X. Zhao, On tension–compression yield asymmetry in an extruded Mg–3Al–1Zn alloy, J. Alloys Comp. 478 (2009) 789–795, http://dx.doi.org/10.1016/j.jallcom.2008.12.033.
[21] A.J. Barnes, Superplastic forming 40 years and still growing, J. Mater. Eng. Perform. 16 (2007) 440–454, http://dx.doi.org/10.1007/s11665-007-9076-5.
[22] T.G. Langdon, An evaluation of the strain contributed by grain boundary sliding in superplasticity, Mater. Sci. Eng. A 174 (1994) 225–230, http://dx.doi.org/10.1016/0921-5093(94)91092-8.
[23] T.G. Langdon, The mechanical properties of superplastic materials, Metall. Trans. A 13 (1982) 689–701, http://dx.doi.org/10.1007/BF02642383.
[24] S.S. Park, B.S. You, Low-temperature superplasticity of extruded Mg–Sn–Al–Zn alloy, Scr. Mater. 65 (2011) 202–205, http://dx.doi.org/10.1016/j.scriptamat.2011.04.005.
[25] R.B. Figueiredo, T.G. Langdon, Strategies for achieving high strain rate superplasticity in magnesium alloys processed by equal-channel angular pressing, Scr. Mater. 61 (2009) 84–87, http://dx.doi.org/10.1016/j.scriptamat.2009.03.012.
[26] W.J. Kim, B.H. Lee, J.B. Lee, M.J. Lee, Y.B. Park, Synthesis of high-strain-rate superplastic magnesium alloy sheets using a high-ratio differential speed rolling technique, Scr. Mater. 63 (2010) 772–775, http://dx.doi.org/10.1016/j.scriptamat.2010.06.011.
[27] S.R. Agnew, J.A. Horton, T.M. Lillo, D.W. Brown, Enhanced ductility in strongly textured magnesium produced by equal channel angular processing, Scr. Mater. 50 (2004) 377–381, http://dx.doi.org/10.1016/j.scriptamat.2003.10.006.
[28] M. Eddahbi, P. Pérez, M.A. Monge, G. Garcés, R. Pareja, P. Adeva, Microstructural characterization of an extruded Mg–Ni–Y–RE alloy processed by equal channel angular extrusion, J. Alloys Comp. 473 (2009) 79–86, http://dx.doi.org/10.1016/j.jallcom.2008.05.064.
[29] R.B. Figueiredo, T.G. Langdon, Principles of grain refinement and superplastic flow in magnesium alloys processed by ECAP, Mater. Sci. Eng. A 501 (2009) 105–114, http://dx.doi.org/10.1016/j.msea.2008.09.058.
[30] G.B. Hamu, D. Eliezer, L. Wagner, The relation between severe plastic deformation microstructure and corrosion behavior of AZ31 magnesium alloy, J. Alloys Comp. 468 (2009) 222–229, http://dx.doi.org/10.1016/j.jallcom.2008.01.084.
[31] E. Mostaed, M. Vedani, M. Hashempour, M. Bestetti, Influence of ECAP process on mechanical and corrosion properties of pure Mg and ZK60 magnesium alloy for biodegradable stent applications, Biomatter 4 (2014) e28283, http://dx.doi.org/10.4161/biom.28283.
[32] T. Mukai, M. Yamanoi, H. Watanabe, K. Higashi, Ductility enhancement in AZ31 magnesium alloy by controlling its grain structure, Scr. Mater. 45 (2001) 89–94, http://dx.doi.org/10.1016/S1359-6462(01)00996-4.
[33] E. Mostaed, Q. Ge, M. Vedani, P.A. De Oliveira Botelho, C. Zanella, F. Deflorian, Investigation on the influence of grain size on strength, ductility, and corrosion properties in Mg and Mg–Zn based alloys for biodegradable stents, Eur. Cell Mater. 26 (2013) 84.
[34] Y. Ogushi, E. Mostaed, D. Dellasega, M. Vedani, H. Miyamoto, H. Fujiwara, Aging behavior of ECAP processed AZ80 Mg alloy, IOP Conf. Ser. Mater. Sci. Eng. 63 (2014) 012076, http://dx.doi.org/10.1088/1757-899X/63/1/012076.
[35] K. Higashi, M. Mabuchi, T.G. Langdon, High-strain-rate superplasticity in metallic materials and the potential for ceramic materials, ISIJ Int. 36 (1996) 1423–1438, http://dx.doi.org/10.2355/isijinternational.36.1423.
[36] R.B. Figueiredo, T.G. Langdon, Record superplastic ductility in a magnesium alloy processed by equal-channel angular pressing, Adv. Eng. Mater. 10 (2008) 37–40, http://dx.doi.org/10.1002/adem.200700315.
[37] Y. Iwahashi, J. Wang, Z. Horita, M. Nemoto, T.G. Langdon, Principle of equal-channel angular pressing for the processing of ultra-fine grained materials, Scr. Mater. 35 (1996) 143–146, http://dx.doi.org/10.1016/1359-6462(96)00107-8.
[38] V.M. Segal, Equal channel angular extrusion: from macromechanics to structure formation, Mater. Sci. Eng. A 271 (1999) 322–333, http://dx.doi.org/10.1016/S0921-5093(99)00248-8.
[39] ASTM E8-04, Test Methods for Tension Testing of Metallic Materials, Annual book of ASTM standards, ASTM, Philadelphia, PA, 2004.
[40] ASTM E9-09, Test Methods of Compression Testing of Metallic Materials at Room Temperature, Annual book of ASTM standards, ASTM, Philadelphia, PA, 2009.
[41] F.-D. Dumitru, O.F. Higuera-Cobos, J.M. Cabrera, ZK60 alloy processed by ECAP: microstructural, physical and mechanical characterization, Mater. Sci. Eng. A 594 (2014) 32–39, http://dx.doi.org/10.1016/j.msea.2013.11.050.
[42] Q. Miao, L. Hu, X. Wang, E. Wang, Grain growth kinetics of a fine-grained AZ31 magnesium alloy produced by hot rolling, J. Alloys Comp. 493 (2010) 87–90, http://dx.doi.org/10.1016/j.jallcom.2009.12.049.
[43] W.B. Hutchinson, M.R. Barnett, Effective values of critical resolved shear stress for slip in polycrystalline magnesium and other hcp metals, Scr. Mater. 63 (2010) 737–740, http://dx.doi.org/10.1016/j.scriptamat.2010.05.047.
[44] M.A. Meyers, O. Vöhringer, V.A. Lubarda, The onset of twinning in metals: a constitutive description, Acta Mater. 49 (2001) 4025–4039, http://dx.doi.org/10.1016/S1359-6454(01)00300-7.
[45] O.D. Sherby, J. Wadsworth, Superplasticity—recent advances and future directions, Prog. Mater. Sci. 33 (1989) 169–221, http://dx.doi.org/10.1016/0079-6425(89)90004-2.